

One-axis Hysteresis Motor Driven Magnetically Suspended Reaction Sphere

Lei Zhou, Mohammad Imani Nejad, David L. Trumper

Department of Mechanical Engineering, Massachusetts Institute of Technology, Cambridge, MA, 02139, USA

Abstract

This paper presents the design, modeling, control and experimental results for a one-axis magnetically suspended reaction sphere (1D-MSRS) driven by a hysteresis motor. The goal of this work is twofold: (a) explore possible designs for magnetically suspended reaction sphere for three-axis spacecraft attitude control, and (b) study the potential of hysteresis motors for the reaction wheel/sphere drives. The 1D-MSRS uses a hysteresis motor with a spherical rotor made of solid steel. The rotor sphere is magnetically suspended in all translational directions, and is driven about the vertical axis by a bearingless hysteresis motor. We present the modeling and control of the magnetic suspensions of the bearingless motor in the 1D-MSRS, and the hysteresis motor dynamics are analyzed by a hysteresis motor equivalent circuit model with the loop-widening effect being considered. The 1D-MSRS system has experimentally demonstrated a starting torque of 8.9 mNm under 0.7 A peak sinusoidal excitation current. With this excitation the sphere can run up to 12,000 rpm synchronously in the presence of air drag. This study demonstrates that the hysteresis motor has strong potential for use in high-speed, low-vibration reaction wheels.

Keywords: magnetic suspension, bearingless motor, hysteresis motor, reaction wheel

1. Introduction

In the flight control of spacecrafts, rotational maneuvering requires an external torque, which is often provided by reaction wheels. To achieve attitude control in all degrees of freedom (DOFs), a minimum of three reaction wheels are typically needed in the system. By accelerating the appropriate wheels, the system can generate a zero-mean torque about any axis to the spacecraft, and the generated momentum can be stored as well [1]. These wheels can also be used for vibration compensation and for orientation control of solar arrays [2].

As an alternative to the reaction wheels, the idea of using a single magnetically suspended reaction sphere (MSRS) for spacecraft attitude control has been investigated by a number of researchers [3, 4, 5, 6, 7, 8]. The vision here is that a sphere can be independently accelerated about any axis by a three-dimensional spherical motor, making the attitude of the spacecraft in all axes controllable by a single device. This torque independence can eliminate gyroscopic coupling as occurs with multiple reaction wheels with fixed rotation axes. In addition, the magnetic suspension eliminates the mechanical friction of the bearings, which relieves the control difficulties due to Coulomb friction when the wheel/sphere speed is crossing zero. The magnetic bearing also allows the device to operate without lubrication and extends the lifetime of the device. Furthermore, by replacing several reaction wheel assemblies with one single device, mass and volume reduction may be achieved.

Although the idea of a MSRS is not new, it remains a challenging problem due to the difficulties of spherical motor design, magnetic suspension, and the combination of the two technologies. One recent MSRS design presents a permanent magnet synchronous motor (PMSM)-based reaction sphere [7, 9].

This design uses tiled magnets on the rotor sphere surface, which enables simpler angular position sensing and control. However, the complexity of the rotor structure may make this design difficult to be used in small satellites, and the strength of the bonded rotor may limit its maximum rotational speed.

Among many motor principles, the hysteresis motor is receiving increasing attention in the past decade due to its advantages of simple structure, vibration-free operation, and self-starting capability. The rotor of a hysteresis motor can be made out of a single piece of hard and strong steel, which will allow the rotor to have very small imbalance. This feature also makes the rotor able to sustain large centrifugal force, which makes the hysteresis motor attractive for high-speed applications. These advantages of hysteresis motor provide the motivation for our study of their use in reaction wheel/sphere applications.

As a first step, we focused this study on the design of a magnetically suspended reaction sphere with one-axis hysteresis drive (1D-MSRS). This paper presents the design characteristics, modeling, control and test results of the 1D-MSRS. The potential of hysteresis motors for reaction wheel applications is also discussed.

This paper is organized as follow. Section 2 presents an introduction to the 1D-MSRS hardware. Section 3 introduces the design and control for the vertical suspension of the reaction sphere. Section 4 describes the bearingless motor subsystem used for the lateral directional suspension of the sphere. Section 5 introduces the hysteresis motor for the 1D-MSRS. Section 6 discusses the comparison between the 1D-MSRS and a commercial reaction wheel. Conclusion and future work is drawn in Section 7.

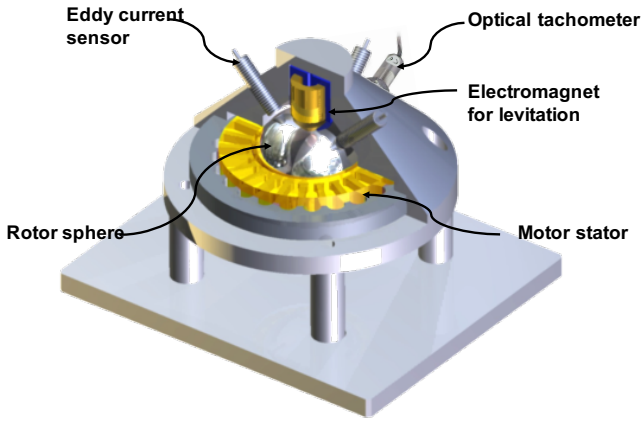


Figure 1: CAD model for the 1D-MSRS.

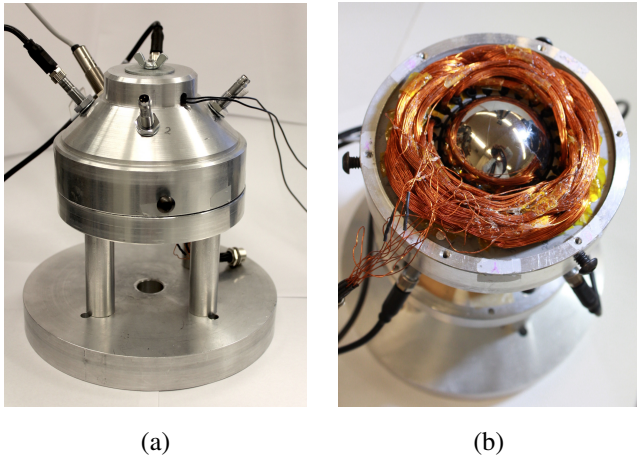


Figure 2: Photographs of the 1D-MSRS.
(a) Structure; (b) stator and rotor.

2. 1D-MSRS hardware overview

The 1D-MSRS demonstrates a hysteresis motor with a spherical rotor made of solid steel, and the rotor is magnetically suspended in all translational directions. Fig. 1 shows a CAD model of the 1D-MSRS, and the photographs of the device are presented in Fig. 2. The rotor in the 1D-MSRS is a solid sphere of hardened D2 steel. Four eddy current sensors are placed around the rotor to measure the sphere's position in three translational DOFs. These sensors are arranged 45° from the vertical axis, and are separated by 90° in the azimuthal coordinate. The rotor sphere is magnetically levitated in the vertical direction by a reluctance actuator placed at its north pole. A stator is arranged around the sphere's equator line, serving both for levitating the sphere in the horizontal plane and for torque generation about the vertical-axis by means of a bearingless motor configuration. A reflective optical tachometer is used for the sphere's speed detection by sensing a black mark on the sphere.

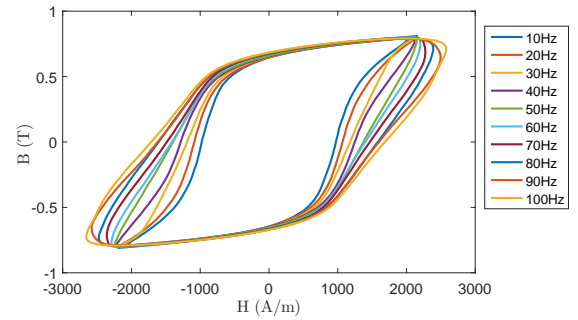


Figure 3: Measured B - H loop for D2 steel ring under different excitation frequencies.

2.1. Rotor

The rotor of the 1D-MSRS is a 54 mm diameter solid sphere of D2 steel. Although materials with larger hysteresis loops exist, we selected D2 steel for the rotor in the 1D-MSRS for the proof of our design. D2 steel is a high Carbon, high Chromium tool steel. It contains 11 to 15 percent Chromium, which makes it a deep hardening, highly wear resistant and magnetically hard alloy. This allows the D2 steel to be used for the rotor of a hysteresis motor. Fig. 3 shows the B - H curve of D2 steel measured under different excitation frequencies while controlling the amplitude of the B field to 0.8 T. It can be seen that the hysteresis loop gets wider as the excitation frequency increases. This effect is known as the "loop widening effect" for hysteresis loops, which is induced by the eddy current in the material. For more details on the measurement of the hysteresis loop see [10].

2.2. Stator

The rotation motor and lateral suspension function are implemented with coils on a stator with 24 slots and a length of 10mm. The stator is constructed by stacking 12 layers of magnetic laminations. In order to reach a compact design, the multiple-winding type bearingless motor is used. This design enables the stator to work as a magnetic bearing and generate a revolving magnetic field simultaneously. The details of the bearingless motor and its modeling and control are presented in Section 4.

2.3. System connection

Fig. 4 shows a hardware connection diagram of the 1D-MSRS. The real-time controller is running at a sampling and control rate of 5 kHz. The signals from the eddy current sensors are collected by the controller through 4 channels of A/D converters. The digital pulses from the optical tachometer are acquired by the digital input channel of the controller, and are transformed into a speed measurement in software. Based on these measurements, the controller computes the control signals at the current sample instant, and sends the signals into seven D/A converters. Seven linear power amplifiers with analog current control loops are used to amplify the control signals and then energize the motor windings and the vertical suspension actuator coil.

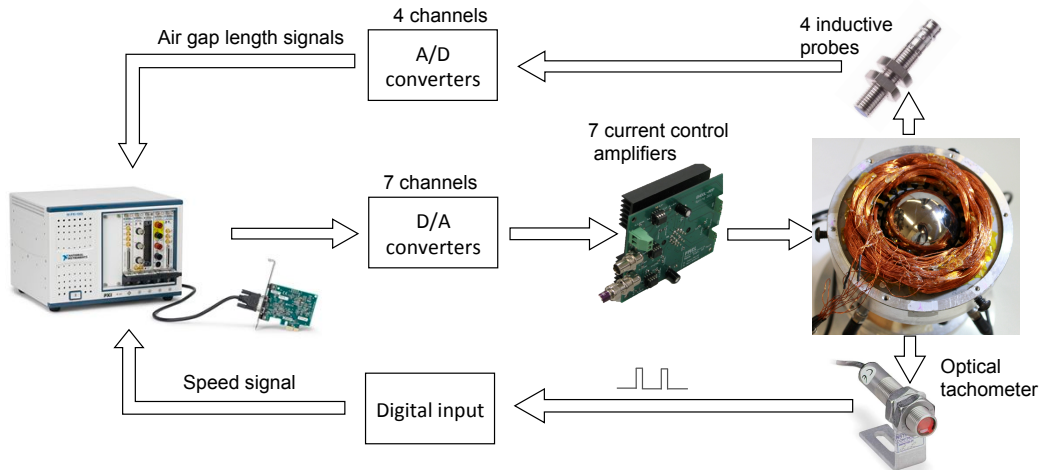


Figure 4: 1D-MSRS hardware connection diagram.



Figure 5: Vertical levitation of sphere by a flux-biased reluctance actuator with an air gap of 0.5 mm. DC current level in the actuator coil is 0.12 A.

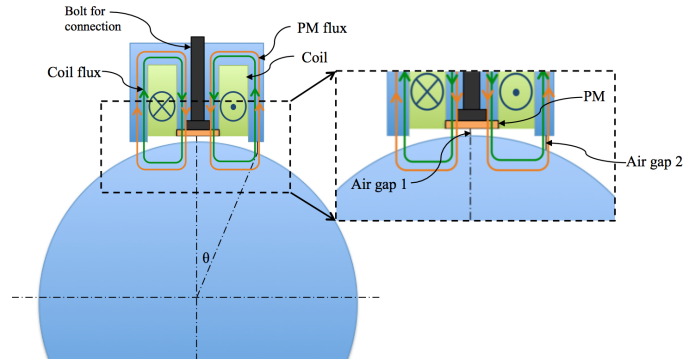


Figure 6: Vertical direction magnetic levitation actuation system. Note biasing permanent magnet (PM) on the central pole face.

The 1D-MSRS consists of three subsystems. They are: 1) a single degree-of-freedom magnetic suspension system for the sphere's vertical suspension, 2) a bearingless motor system for the sphere's lateral suspension, and 3) a hysteresis motor for driving the sphere about the vertical axis. In the design and analysis of the 1D-MSRS, these three subsystems are considered to be decoupled, that is, the interactions between the subsystems are treated as disturbances. In the following sections, the design, modeling, control and test results of each subsystem are introduced.

3. Vertical suspension of reaction sphere

This section briefly introduces the vertical direction magnetic suspension of the sphere. Fig. 5 shows a photograph of the sphere being magnetically levitated in the vertical direction by a reluctance actuator arranged on top of the sphere with an air gap of 0.5 mm.

In the vertical magnetic suspension system, the magnetic force generated by the reluctance actuator must compensate the weight of the sphere, which requires a relatively high DC

current level in the actuator coil. In order to make the system more energy efficient, a flux-biased reluctance actuator is designed for the vertical suspension, where a disk-shape permanent magnet (PM) is arranged in the magnetic path of the reluctance actuator to add a bias flux. The magnet is relatively thin, so the additional reluctance in the actuator magnetic circuit is acceptable. Fig. 6 shows a cross-section diagram of the magnetic suspension of the reaction sphere. With the flux-biased actuator design, the required DC current level in the actuator coil is reduced to 0.12 A, while a non-biased actuator of the same geometry requires a DC current of 0.85 A for levitating the sphere.

In addition to the PM bias flux, the coil in the actuator slot is excited with controlling current to stabilize the magnetic suspension of the sphere. In the 1D-MSRS device, the vertical position of the sphere is measured by taking the average of the signals from the four eddy current sensors. A PID controller is implemented in the real-time controller to stabilize this magnetic suspension control loop. A cross-over frequency of 320 rad/s is reached for this magnetic suspension control loop, with a phase margin of 40°.

Table 1: Design parameters of the bearingless motor in 1D-MSRS

parameter	value
Rotor sphere radius	27 mm
Stator height	10 mm
Nominal air gap length	0.5 mm
Stator number of slots	24
Number of poles for motor winding	4
Number of turns per slot for motor winding	80
Number of poles for suspension winding	2
Number of turns per slot for suspension winding	40

4. Bearingless motor

In the 1D-MSRS, the magnetic suspension of the rotor sphere in the lateral directions is achieved by a bearingless motor. The bearingless motor has two sets of windings arranged on a single stator. By correctly configuring and controlling the currents in these windings, the machine can generate radial forces for rotor's lateral suspension as well as a rotational magnetic field for spinning the rotor. Readers are referred to [11] for more details on bearingless motors. In the stator of the 1D-MSRS, two sets of three-phase windings, 4-pole and 2-pole, are used, where the 4-pole windings are the motor windings, and the 2-pole windings are the suspension control windings. Table 1 presents the design parameters of the bearingless motor in the 1D-MSRS.

Fig. 7 shows a block diagram of the bearingless motor control system in the 1D-MSRS. By exciting the motor windings (the 4-pole windings) with symmetrical three-phase currents, a revolving magnetic field is generated to rotate the sphere. The radial displacements of the rotor in the stationary frame are measured by the eddy current sensors to provide feedback for suspension control. Two independent PID controllers are designed for the magnetic suspension in x- and y-direction in the stationary frame, and the control effort signals u_x, u_y are transformed to the rotational three-phase coordinates by means of Park and Clarke transformations [11]. These transformed control signals are then fed into the current control power amplifiers to energize the suspension control windings (the 2-pole windings). The controlling magnetic field generated by the suspension windings, together with the motor fields, produces the radial suspension forces on the rotor sphere. As is shown in Fig. 7, in a bearingless motor system, the control inputs are the currents in the 2-pole windings in the stationary frame u_x and u_y , while the output signals of system are the radial displacements of the rotor in stationary x- and y-directions.

4.1. Lateral suspension system modeling and identification

To stabilize the lateral suspension of the reaction sphere, a dynamic model of the bearingless motor system needs to be established and identified for control design purposes. In this section, the modeling and testing of the suspension characteristics of the bearingless motor in the 1D-MSRS are discussed.

These characteristics are also shared by other cylindrical rotor AC bearingless motors.

In a bearingless motor system, the suspension forces are generated by the interaction between the motor magnetic field and the suspension control magnetic field. A bearingless motor can be viewed as a "flux-steering" device, where the magnetic fluxes generated by the motor windings are steered by the controlling fluxes in a rotating frame to generate the radial suspension control forces. (See [12] for an introduction to the principles for "flux-steering" magnetic designs.) As a result, the radial suspension system dynamics in a bearingless motor are highly dependent on the current level in the motor windings. A limiting example is that if there is no current in the motor windings, no suspension forces can be produced.

In this study, we derived an analytical model for the lateral suspension of the reaction sphere in the bearingless motor system under the assumption that reluctance force dominate the suspension forces. The detailed derivations of these results are presented in [13]. By linearizing the dynamic equation of the rotor in the model, a transfer function model from the equivalent two-phase suspension winding current in the stationary frame (signal $u_x(t)$ in Fig. 7) to the rotor's x-directional radial displacement (signal $x(t)$ in Fig. 7) can be found as

$$\frac{X(s)}{U_x(s)} = \frac{K_i}{ms^2 - K_s}, \quad (1)$$

where m is the mass of the rotor sphere, and K_s and K_i are the negative stiffness and the force constant of the bearingless motor suspension system, respectively. Note that the sign in front of K_s is negative. This negative stiffness is associated with the open-loop plant instability, such that the rotor is unstable at the stator center bore when the system is in open-loop. Constants K_s and K_i can be calculated as

$$K_s = \frac{3}{\pi} \frac{\mu_0 R l N_4^2}{g_0^3} I_m^2 [N/m], \quad (2a)$$

$$K_i = \frac{\sqrt{6}}{\pi} \frac{\mu_0 R l N_2 N_4}{g_0^2} I_m [N/A], \quad (2b)$$

where I_m is the zero-to-peak current amplitude of the AC current in the 4-pole motor windings, N_4 and N_2 are the numbers of turns per phase per pole of the 4-pole and 2-pole windings, respectively, g_0 is the nominal air gap length, R is the radius of the rotor sphere, l is the stator height in the axial direction, and μ_0 is the permeability of free space.

It can be seen from (1) and (2) that the system dynamics of a bearingless motor depend on the motor winding current amplitude I_m . This observation can be verified by measuring the frequency response of the lateral suspension system in the 1D-MSRS under different motor winding current amplitudes. The measured plant Bode plots of the reaction sphere lateral suspension system are depicted in Fig. 8. Note that this plant measurement was taken while under closed-loop control, since the open-loop system is unstable. From Fig. 8 we conclude that the system dynamics are getting faster as the excitation amplitude I_m increases, consistent with the increase of K_s with I_m in (2).

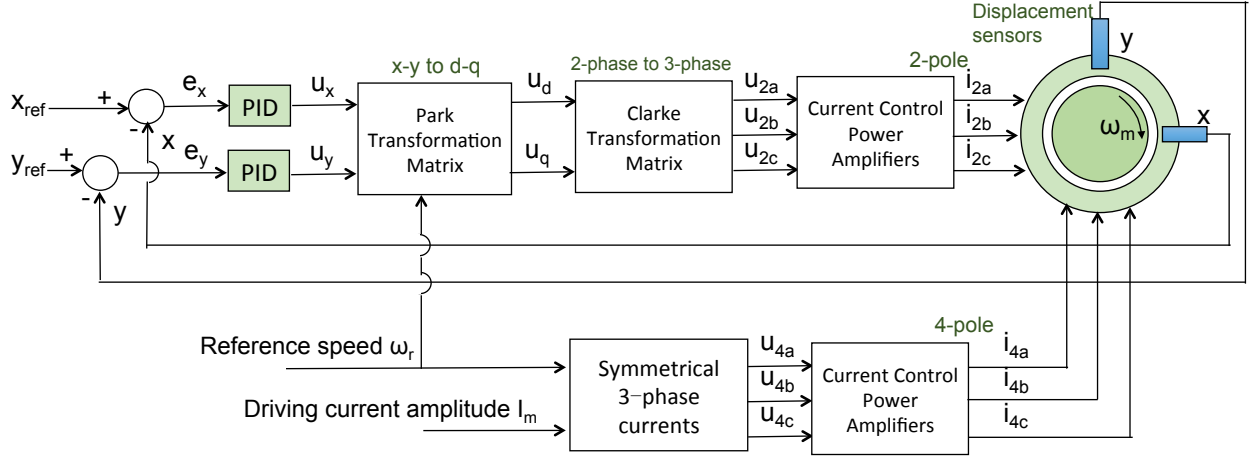


Figure 7: Bearingless motor control block diagram.

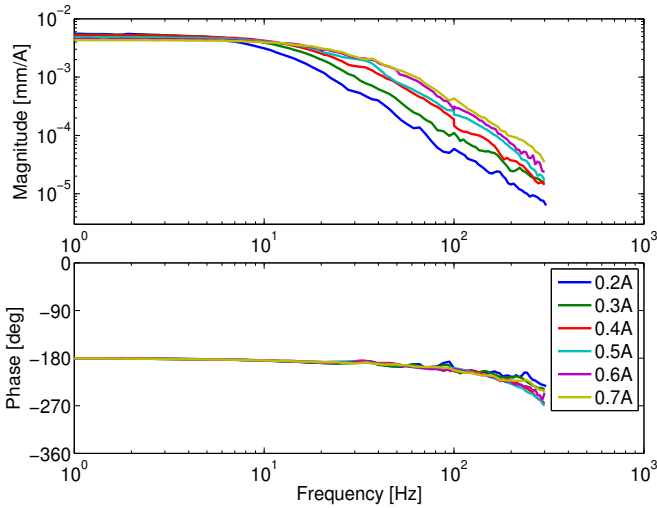


Figure 8: Experimentally measured Bode plot response for x-direction sphere suspension with different motor winding current amplitudes (zero-to-peak).

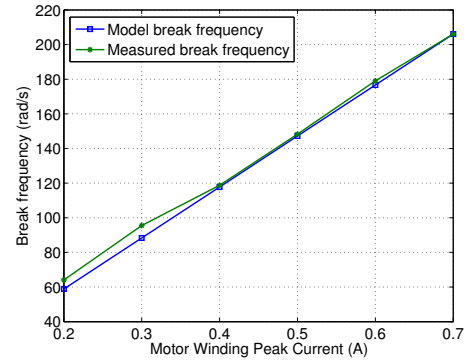


Figure 9: Break frequency of plant with different motor winding current amplitude.

Fig. 9 shows the break frequency of the measured bearingless motor plant Bode plots in Fig. 8 and the modeled break frequency given by (1) and (2). Good match between the modeled and the experimental measured data verifies the transfer function model of bearingless motors given in (1) and (2).

4.2. Lateral suspension control design

When a bearingless motor is used for reaction wheel/sphere application, its motor winding current amplitude needs to vary according to the torque requirements. This fact requires the lateral suspension controllers for the 1D-MSRS to take care of this system dynamics variation and still be able to stabilize the magnetic suspension control under all excitation conditions.

The loop-shaping method is used to design the lateral suspension controllers for the 1D-MSRS based on the plant dynamic model. Since the plant system dynamics of the bearingless motor are varying with the motor winding current amplitude I_m , we use I_m as a gain scheduling parameter. Lead-lag form PID controllers are used for the lateral suspension control, and the

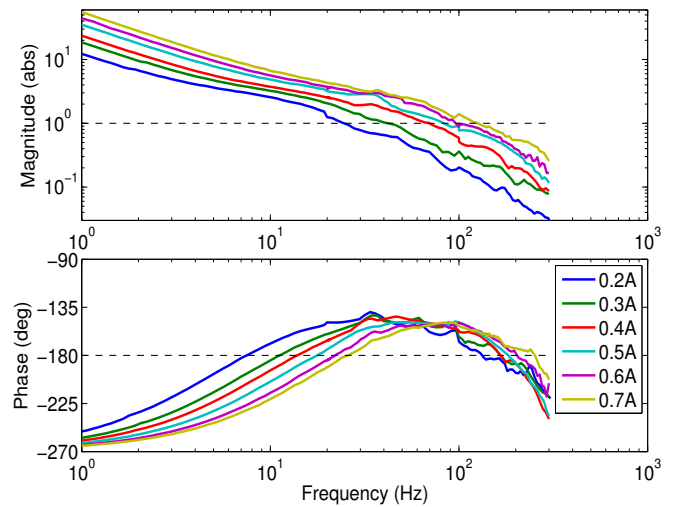


Figure 10: Measured loop-return-ratio Bode plots of the lateral suspension control loop under different motor winding peak current amplitudes.

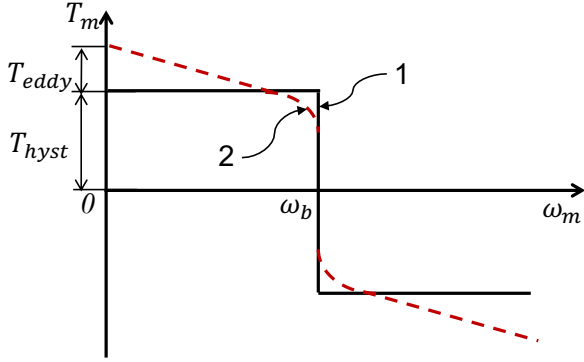


Figure 11: Typical hysteresis motor torque-speed curve. The curve 1 (black solid line) shows an ideal hysteresis motor torque-speed curve, and the curve 2 (red dash line) shows a practical hysteresis motor torque-speed curve, where the effect of eddy current is taken into account.

controller gains are designed to vary according to the parameter I_m . The design goal is to maintain a constant phase margin and therefore keep the loop robustly stable.

Fig. 10 shows the measured loop-return-ratio Bode plot of the x-directional suspension control of the reaction sphere. With the gain scheduling controller design, the control loop has a cross-over frequency which varies with the motor current amplitude, and an approximately fixed phase margin of about 40° . Under 0.2 A excitation current, the loop has a crossover frequency of 170 rad/s. With 0.7 A excitation, the crossover frequency is 620 rad/s. With this approach, the radial position of the sphere is successfully regulated at the center of the stator under varying motor current amplitude.

5. Hysteresis motor for reaction sphere

The 1D-MSRS uses a hysteresis motor for its motor drive around the vertical axis. A hysteresis motor operates by the magnetic hysteresis effect of its rotor material. Since the magnetization produced in the ferromagnetic material lags behind the magnetizing force, a torque is generated due to the rotor and stator field interaction. In addition, eddy currents in the rotor also produce torque when the motor is operating asynchronously [14]. Loosely speaking, a hysteresis motor can be described as a combination of a weak permanent magnet motor and an solid rotor induction motor. However, modeling of this motor is more complicated, since the magnetization of the rotor moves under stator excitation relative to the rotor material.

Fig. 11 shows a typical hysteresis motor torque-speed curve, where the curve 1 in the black solid line shows the ideal hysteresis motor torque-speed relationship, and the curve 2 in the red dash line is a practical torque-speed curve with the eddy current effect included. It can be seen that the ideal hysteresis motor demonstrates constant hysteresis torque T_{hyst} during asynchronous operation, where the motor speed ω_m does not equal the stator base speed ω_b . When the rotor is conductive, the eddy current in the rotor also helps the torque generation, which gives the frequency-dependent eddy current torque T_{eddy} . At the synchronous speed, the motor torque is solely due to the

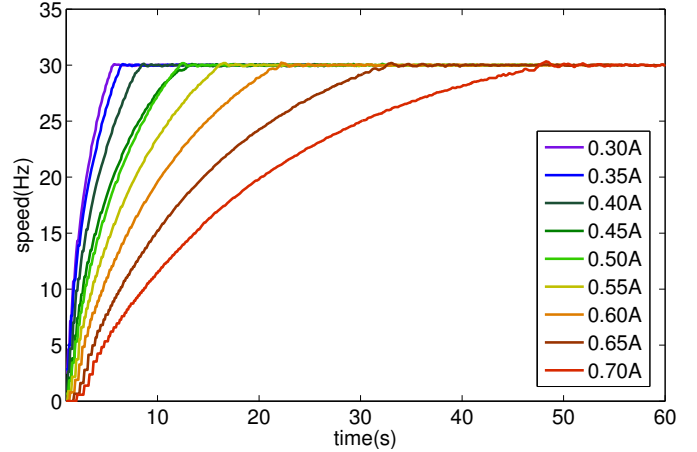


Figure 12: Acceleration curves of 1D-MSRS under different excitation current amplitude.

hysteresis effect, and can demonstrate different values, depending on the load torque and the motor excitation conditions.

5.1. Motor hardware and experimental results

The motor drive in the 1D-MSRS is tested under different motor winding current levels. Fig. 12 shows the start-up speed curves of the 1D-MSRS. In these tests, the motor windings are excited with constant frequency three-phase currents of different amplitudes. It can be seen that all curves lock into the synchronous speed of 30 Hz (1,800 rpm) after acceleration. Data shows that under 0.7 A excitation current, the sphere reaches the synchronous speed of 30 Hz (1,800 rpm) within 6 seconds, with an associated starting torque of 8.9×10^{-3} Nm.

The maximum achievable speed for the 1D-MSRS is also tested. When the motor is excited with 0.7 A current amplitude and when it is running in the lab in the presence of air drag, the sphere can run up to 200 Hz (12,000 rpm) synchronous speed. This motor speed limit is potentially much higher when the sphere is running in vacuum.

5.2. Motor model in the 1D-MSRS

In order to study the physics of the hysteresis motor in the 1D-MSRS and also to provide a simulation tool for future design, a model of the hysteresis motor derived from the fundamental electromagnetics is used to study the motor dynamics of the 1D-MSRS. Modeling of the hysteresis motor is challenging due to the nonlinearity of hysteresis material properties. Through the years, several different models have been developed to calculate the hysteresis motor torque. Reference [15] studies the hysteresis motor by comparing it to the permanent magnet motors, and a hysteresis motor model using analogy to induction motor was proposed in [16]. Although simple and easy to parametrize, these models are not derived from the fundamental electromagnetics and do not provide physical insights. A parallelogram-shaped simplification for the hysteresis loop has been proposed in [17], and an equivalent circuit model for the hysteresis motor based on this assumption was introduced. An alternative hysteresis motor equivalent circuit model

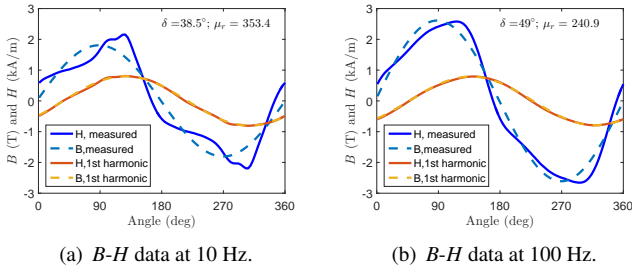


Figure 13: Measured B and H data and their fundamental harmonics.

based on an elliptical hysteresis loop assumption was proposed in [18], where only the fundamental harmonics of the motor field are considered. Recent work extended this model to include the eddy current torque by considering the loop-widening effect for the hysteresis loop [19].

In all these models mentioned above, the dynamics of the hysteresis motor, which includes both the synchronous and the asynchronous operation modes, are not encompassed. This is due to the “torque singularity” of the hysteresis motors. As shown in Fig. 11, the hysteresis motor torque at the synchronous speed can demonstrate multiple values. For a hysteresis motor, during the transition from the asynchronous mode to the synchronous operation, the rotor material particles experience minor hysteresis loops, which are difficult to model. To our knowledge, few works have studied the transient behavior for hysteresis motors. Reference [20] studies the equivalent circuit model based on the elliptical hysteresis model for both the synchronous and asynchronous operation of the hysteresis motor, and assumes that the magnetic poles are fixed on the rotor surface once the motor reaches synchronous speed. This assumption ignores the hysteresis losses in the rotor during synchronous operation, which means the modeled hysteresis motor has zero hysteresis damping in synchronous operation, and demonstrates more sustained hunting than a hysteresis motor in practice. However, this model allows us to study the “worst case” hysteresis motor dynamics in both asynchronous and synchronous mode.

In this paper, the hysteresis motor equivalent circuit model based on the elliptical hysteresis loop assumption [18] was selected to calculate the motor torque in the 1D-MSRS. The eddy current torque in the motor was modeled by including the loop-widening effect in the hysteresis model, which allows us to model the torque generation in asynchronous mode with better accuracy. For the synchronous operation mode, the model proposed in [20] was used to study the “worst case” hunting behavior.

We briefly introduce the elliptical-hysteresis-loop-based equivalent circuit model for hysteresis motors from [18] to make this paper self-contained. Readers are referred to [18] for the derivation for the model from fundamental electromagnetics. In this model, symmetric three-phase current excitation is assumed. The B-H curve of the rotor material is approximated

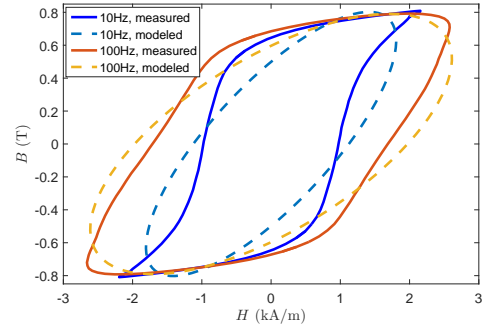


Figure 14: Elliptical approximation of the hysteresis loop of D2 steel under 10 Hz and 100 Hz.

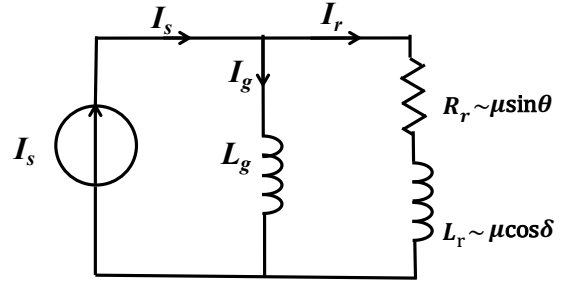


Figure 15: Equivalent circuit model of hysteresis motor.

by an ellipse, which can be described by

$$\begin{aligned} B &= B_m \cos \theta, \\ H &= \frac{B_m}{\mu} \cos(\theta + \delta_m), \end{aligned} \quad (3)$$

where B_m is the maximum amplitude of the flux density, and δ_m is the lag angle between H and B . The permeability of the rotor material μ is defined as the ratio of the maximum values of B and H , that is, $\mu = B_m/H_m$, where H_m is the maximum field intensity. This model of the magnetic hysteresis is also known as complex permeability model [21]. This model considers only the fundamental harmonics for B and H , and all higher order harmonics are neglected. Fig. 13 shows the measured B - H data of the D2 steel at 10 Hz and 100 Hz and their fundamental harmonics. In the measurement the magnitude of the B field is regulated to a constant 0.8 T. Fig. 14 shows the hysteresis loops of the D2 steel at 10 Hz and 100 Hz, and their elliptical approximations. Note that the hysteresis loop gets wider as the excitation frequency increases due to the eddy current in the rotor.

The elliptical approximation of the hysteresis loop allows us to use a linear equivalent circuit to analyze the motor system. Fig. 15 shows the hysteresis motor equivalent circuit for the 1D-MSRS. In this model the stator resistance and inductance are not included because for motor in the 1D-MSRS uses current controlled amplifiers. In Fig. 15, I_s is the stator current, I_g is the apparent air-gap current, and I_r is the apparent rotor current. Notice that these apparent currents are not real currents that flow in the air-gap or in rotor. Instead, they are a part of the stator current that flows in the model circuit if Fig. 15. The

values of the circuit elements can be calculated by

$$L_g = \frac{2mK_w^2 N^2 \mu_0 l r_g}{p^2 \pi g_0}, \quad (4)$$

$$R_r = \omega_b \frac{mK_w^2 N^2 V_r \mu}{\pi^2 r_r^2} \sin \delta, \quad (5)$$

$$L_r = \frac{mK_w^2 N^2 V_r \mu}{\pi^2 r_r^2} \cos \delta. \quad (6)$$

Here δ is the separation angle between the B -field and H -field in the rotor material, K_w is the winding factor, m is the number of phase, p is the number of poles, r_r is mean radius of length of the magnetic field path within rotor, r_g is the mean radius of the air gap, ω_b is the input synchronous speed, N is the number of windings per phase, g_0 is the air-gap length, μ is the permeability of the rotor material, and V_r is the effective rotor volume.

The apparent current values can be solved from the equivalent circuit model shown in Fig. 15. The motor electrical torque can then be calculated by [18]

$$T_e = \frac{m p}{2} L_g I_r I_g \sin \delta. \quad (7)$$

The rotor speed can be found from the mechanical dynamic equation for the rotor as

$$\frac{J d\omega_r}{p dt} = T_e - A|\omega_r|\omega_r, \quad (8)$$

where A is the coefficient of the air drag torque, and J is the rotor inertia.

Recall that the angle δ is the spatial separation angle between the B -field and H -field in the rotor material, which cannot exceed the lag angle of the rotor material hysteresis loop δ_m . Therefore the angle δ satisfies the constraint

$$-\delta_m < \delta < \delta_m, \quad (9)$$

where δ_m is the hysteresis loop lag angle given in Eq. (3). When the hysteresis motor is operating in asynchronous mode, the lag angle is equal to its maximum, which is δ_m .

To include the motor torque generated by the eddy currents in the rotor, the loop-widening effect of the hysteresis loop can be taken into account. There are two parameters for the elliptical hysteresis model: μ and δ_m . Both parameters are varying with the excitation frequency of the magnetic field. Fig. 16 shows the measured and fitted variation of μ and δ_m with respect to frequency at a constant flux density amplitude. It is shown that both the parameters are varying with the measurement frequency approximately linearly. In the hysteresis motor equivalent circuit model, the hysteresis model parameters μ and δ_m can be selected as identified linear functions of the slip frequency, which is the difference between the stator field frequency ω_b and the rotor's mechanical frequency ω_r . In this way the eddy current torque generation in the hysteresis motor can be modeled.

When the rotor's mechanical speed reaches the vicinity of synchronous speed, the rotor magnetic pole aligns with the rotor mechanical angle. Under the assumption of the magnetic poles

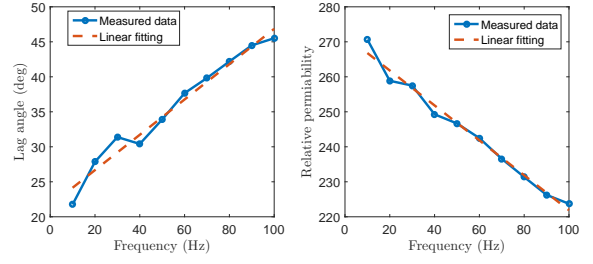


Figure 16: Hysteresis parameters of D2 steel under different frequencies at 0.8 T amplitude. Left: lag angle. Right: relative permeability.

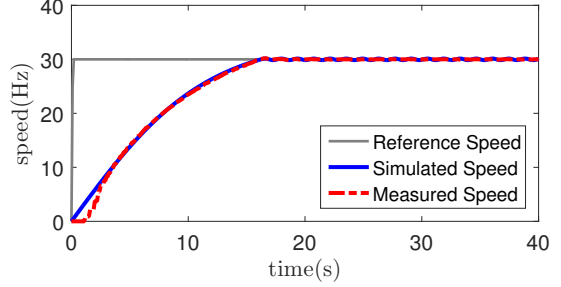


Figure 17: Measured and simulated 1D-MSRS speed under excitation current of 0.45A.

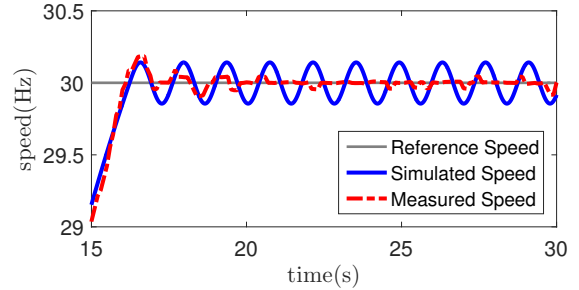


Figure 18: Zoomed in measured and simulated 1D-MSRS speed under excitation current of 0.45A.

of the rotor are not moving with respect to the rotor material after the motor reaches synchrony, the angle δ can be updated by the dynamic equation

$$\frac{d\delta}{dt} = \frac{\omega_b - \omega_r}{p}. \quad (10)$$

Introducing Eq. (9) and (10) in the hysteresis motor equivalent circuit model allows the model to describe the motor behavior in both synchronous and asynchronous operation. As was discussed in [20], when the motor slip is large, the constraint in (9) is activated, and the angle δ always equal to δ_m . As a result, the motor can produce a constant hysteresis torque and an eddy current torque that is changing with slip frequency. When the rotor speed is close to the synchronous speed, (10) is activated to describe the dynamics of angle δ , which models the hunting behavior of the hysteresis motor.

Numerical simulations of the hysteresis motor in the 1D-MSRS were conducted by solving the equivalent circuit model and using (4-8) with the hysteresis parameters μ and δ being functions of the slip frequency. Fig. 17 shows the simulated and experimental measured motor starting speed data plotted together, and Fig. 18 shows the zoomed in speed data around

Table 2: Torque simulation results with different rotor material properties. AlNiCo rotor material data taken from [22].

Material	μ_r	δ [deg]	Hysteresis torque at 0.7 A excitation [mNm]
D2 steel	350	40	4.15
AlNiCo ($H_c = 11.1$ kA/m)	60	42	14.9
AlNiCo ($H_c = 15.9$ kA/m)	45	48	16.2

the synchronous speed. It can be seen that the simulation and the experimental data align well in the accelerating transient. However, when the motor reaches synchronous speed, the simulated speed data demonstrates a less damped speed hunting behavior than the experimental measured speed data.

5.3. Speculation on performance with other rotor materials

Although only one kind of rotor material, D2 steel, has been tested in the 1D-MSRS hardware, the model of the hysteresis motor presented in the previous section allows us to estimate the motor performance with other rotor materials. Table 2 presents the complex permeability values of two different kinds of semi-hard AlNiCo magnetic materials [22], which are commonly used in hysteresis motor rotors, along with predicted resulted torque.

5.4. Hysteresis motor speed control

When a hysteresis motor is operating, a speed fluctuation slightly above and below the reference speed can be observed when the motor speed reaches synchronous speed, as is seen in Fig. 18. This motor dynamics is known as hunting [23]. It is undesirable when a hysteresis motor is used in a reaction wheel or a reaction sphere, as it will introduce vibrations to the spacecraft via the associated oscillatory torque.

To suppress the motor hunting, a feedback loop on the sphere's rotational speed can be designed and implemented for the 1D-MSRS. Fig. 19 shows a block diagram of the speed control loop. The sphere speed ω_r is measured by an optical tachometer. The input signal to the controller is the speed error e_ω between the desired synchronous speed ω_b and the measured speed ω_r . The control effort signal is defined as the zero-to-peak amplitude of the three-phase excitation current signal I_m . In this analysis let us call it u , denoting the control effort. Note that in this system the value of u is non-negative, and it cannot go below 0.2 A in order to maintain the lateral suspension of the sphere. Also note that in this control system a positive control effort provides decelerating torque when e_ω is negative.

When the reaction sphere is accelerating, it is desired that the motor can catch up with the reference speed, or the synchronous speed, as fast as possible. In optimal control, the minimum time problem with the presence of constraints for control effort can be solved, and the result shows that a bang-bang controller is the

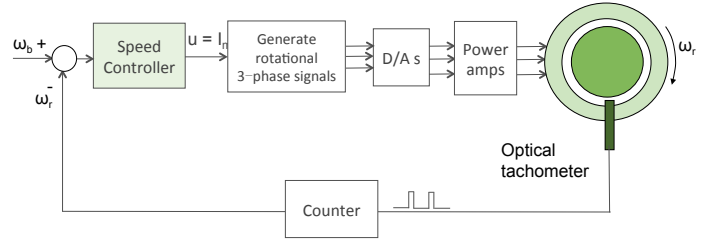


Figure 19: Block diagram of the reaction sphere speed control loop.

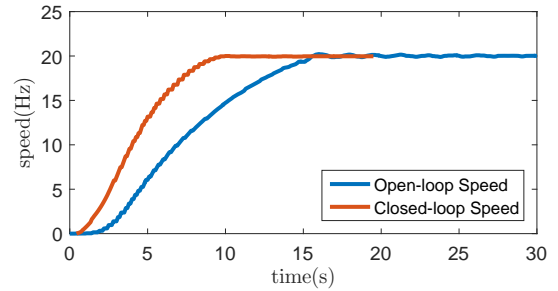


Figure 20: A comparison of experimental open-loop step response speed data and the closed-loop step responses speed data of reaction sphere. The open-loop step response is measured under a peak current value of 0.35 A.

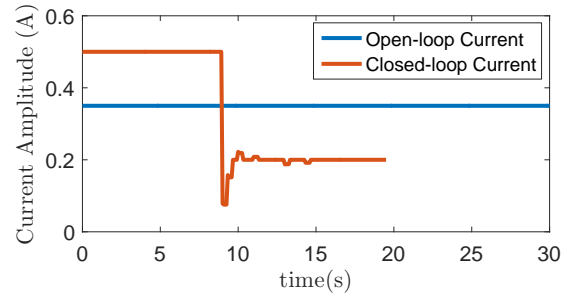


Figure 21: Open-loop and closed-loop control effort data (peak amplitude for motor currents).

best mechanism for achieving minimum speed rise time [24]. For the 1D-MSRS, this requires the motor to operate in open-loop with the maximum allowed excitation amplitude, which enables the motor to accelerate with its maximum ability.

In order to add active damping to the system to suppress the hunting, a lead filter is used as the speed controller when the hunting is happening. Define the maximum available control effort as u_{max} . The speed control law of the 1D-MSRS can be written as

$$u = \begin{cases} u_{max} & \text{if } e_\omega > \Delta \text{ or } e_\omega < -\Delta, \\ u_{PD} & \text{if } -\Delta \leq e_\omega \leq \Delta, \end{cases} \quad (11)$$

where Δ is a constant positive number that sets the threshold of the controller change.

The parameters of the PD controller are determined by the characteristics of the hunting dynamics. For the 1D-MSRS hardware, the motor hunting is at a frequency of 3.9 rad/s. Targeting at damping out this oscillation, the PD compensator for

the reaction sphere's speed regulation was designed as

$$\frac{u_{PD}(s)}{e_{\omega}(s)} = 3.5 \frac{0.4s + 1}{0.04s + 1}. \quad (12)$$

The speed controller given in Eq. (11) and (12) was implemented for the 1D-MSRS. Fig. 17 shows a comparison between the experimental measured open-loop transient speed data and the closed-loop controlled speed data. The open-loop data was measured with $I_m = 0.35$ A, and the maximum allowed control effort was set to be 0.5 A. It can be seen from Fig. 17 that the closed-loop speed has much less oscillation when the speed enters synchrony. This verifies that the designed speed control scheme can effectively suppress the motor hunting. The corresponding motor winding current signals are presented in Fig. 18. With closed-loop control, the motor current peak value reduced to 0.2 A when the reaction sphere is operating in steady state, which allows less energy loss at steady state operation. Experiment shows that when operating in steady state at 1,800 rpm, the power consumption of the 1D-MSRS, including both rotation and lateral magnetic suspension (not including magnetic suspension in vertical direction), is 3.44 W.

6. Discussion

A comparison between the test results of the 1D-MSRS and the specifications of a commercial reaction wheel assembly for typical small satellites is performed, as is shown in Table 3. Here the MicroWheel 200 (MW200) Reaction Wheel from Microsat Systems Canada Inc. [25] is chosen as a benchmark, which has a similar size to the 1D-MSRS prototype.

Data in Table 3 shows that the torque capacity of 1D-MSRS is smaller than that of the MW200 reaction wheel. The reason, to our understanding, is threefold. First, hysteresis motors are not winning in their torque ability comparing with their permanent magnet motor counterparts. Second, D2 steel is not the best rotor material for hysteresis motors. The simulation results presented in Section 5.3 show that larger torque ability can be achieved if the rotor has a better hysteresis property. Third, in the design of the 1D-MSRS, the effective surface area on the rotor for torque production is small, since the stator height was relatively small.

Comparing with MW200 reaction wheel, the 1D-MSRS demonstrated smaller rotor imbalance. In fact, the imbalance of the 1D-MSRS can achieve zero because the uniformity of rotor material and the spherical symmetry of rotor. Besides, the 1D-MSRS has a larger angular momentum capacity since it can run up to a higher synchronous rotational speed. We believe that the sphere can reach a higher synchronous speed when running in vacuum, where the air drag can be eliminated as well. In addition, the 1D-MSRS demonstrated lower power consumption when operating in steady state. This is a direct result of magnetic suspension which eliminated mechanical friction. This comparison demonstrated a good potential of hysteresis motors for the development of high speed, low vibration reaction wheels/spheres, especially when they are assisted with magnetic suspension.

7. Conclusions and future work

The design and development of a hysteresis motor driven magnetically suspended one-axis reaction sphere is presented in this paper. Magnetic suspension, bearingless drive and hysteresis motor principles are used in the design of the 1D-MSRS. An analytical dynamic model of the bearingless motor suspension system is derived and used for the suspension control design. An equivalent circuit model for hysteresis motors is used to analyze the motor dynamics of the 1D-MSRS, and a speed control loop is built for the system to suppress hunting. The 1D-MSRS can run up to 200 Hz (12,000 rpm) in the presence of air drag, and a starting torque of 8.9 mNm is generated with 0.7 A excitation current amplitude. This study demonstrated that the hysteresis motor has a good potential for reaction wheel/sphere applications.

Future work should consider the design and development of a three-axes magnetically suspended reaction sphere (3D-MSRS). Discussions of the possible motor concepts and possible magnetic pole configuration designs for a 3D-MSRS are presented in [13]. In addition, the performance of the 1D-MSRS demonstrates that the hysteresis motor has the potential for the circumstances where quiet operation and high speed are needed. We believe that this motor concept is promising for high speed, low vibration reaction wheel applications.

Acknowledgements

We thank National Instruments for contributing the real-time controller. We thank Professor Wolfgang Gruber at JKU, Linz for the valuable discussions, and thank Dietmar Andessner at JKU, Linz for his help with the hysteresis measurements.

This work is supported by the MIT Lincoln Laboratory via the Advanced Concepts Committee. We also thank Frederick Knight and Andrew Stimac of Lincoln Laboratory for their assistance with this project.

References

- [1] B. Bialke, High fidelity mathematical modeling of reaction wheel performance, *Guidance and control* 1998 (1998) 483–496.
- [2] T. Fukada, H. Hosokai, N. Yajima, Flexibility control of solar battery arrays: 3rd report vibration and attitude control with consideration of the dynamics of a reaction wheel as an actuator, *Bulletin of JSME* 29 (255) (1986) 3121–3125.
- [3] R. D. Ormsby, Capabilities and limitations of reaction spheres for attitude control, *ARS Journal* 31 (6) (1961) 808–812.
- [4] T. E. Tierney, R. J. Curran, Development of an electrostatic suspension reaction sphere, Tech. rep., SAE Technical Paper (1964).
- [5] W. H. Isely, Magnetically supported and torqued momentum reaction sphere, US Patent 4,611,863 (Sep. 16 1986).
- [6] T. Nakanishi, Y. Ando, K. Sakakibara, Electric motor having a spherical rotor and its application apparatus, uS Patent 5,413,010 (May 9 1995).
- [7] E. Onillon, O. Chételat, L. Rossini, L. Lisowski, S. Droz, J. Moerschell, Reaction sphere for attitude control, in: *Proc. 13th European Space Mechanisms and Tribology Symposium*, 2009.
- [8] J. Chabot, H. Schaub, Spherical magnetic dipole actuator for spacecraft attitude control, *Journal of Guidance, Control, and Dynamics* (2016) 911–915.

Table 3: Specifications for MicroWheel 200 (MW200) Reaction Wheel from Microsat Systems Canada Inc.

Specification	MSCI MW200 [25]	1D-MSRS
Size	100 × 90 × 90 mm	120 × 120 × 110 mm
Mass	1.0 kg (assembly for one wheel)	0.63 kg (rotor)+0.42 kg (Stator + vertical suspension actuator)
Imbalance	Static: < 0.2 mg.m; Dynamic: < 0.03 mg.m ²	Almost zero due to rotor's spherical symmetry and magnetic suspension
Torque capacity	26 mNm	8.9 mNm under 0.7 A excitation
Angular momentum capacity	0.18 Nms	0.23 Nms (synchronously at 150 Hz / 9,000 rpm)
Motor power consumption	0 rpm: 3.0 W; 1,800 rpm: 5.5 W;	Operating in steady state at 1,800 rpm: 3.44 W

- [9] L. Rossini, O. Chélat, E. Onillon, Y. Perriard, Force and torque analytical models of a reaction sphere actuator based on spherical harmonic rotation and decomposition, *Mechatronics, IEEE/ASME Transactions on* 18 (3) (2013) 1006–1018.
- [10] D. Andessner, R. Kobler, J. Passenbrunner, W. Amrhein, Measurement of the magnetic characteristics of soft magnetic materials with the use of an iterative learning control algorithm, in: 2011 IEEE Vehicle Power and Propulsion Conference, IEEE, 2011, pp. 1–6.
- [11] A. Chiba, T. Fukao, O. Ichikawa, M. Oshima, M. Takemoto, D. G. Dorrell, *Magnetic bearings and bearingless drives*, Elsevier, 2005.
- [12] X. Lu, et al., Electromagnetically-driven ultra-fast tool servos for diamond turning, Ph.D. thesis, Department of Mechanical Engineering, Massachusetts Institute of Technology (2005).
- [13] L. Zhou, Magnetically suspended reaction sphere with one-axis hysteresis drive, Master's thesis, Mechanical Engineering, Massachusetts Institute of Technology (2014).
- [14] B. R. Teare, Theory of hysteresis-motor torque, *Electrical Engineering* 59 (12) (1940) 907–912.
- [15] M. A. Rahman, Analytical models for polyphase hysteresis motor, *IEEE Transactions on Power Apparatus and Systems* (1) (1973) 237–242.
- [16] D. O'Kelly, Theory and performance of solid-rotor induction and hysteresis machines, in: *Proceedings of the Institution of Electrical Engineers*, Vol. 123, IET, 1976, pp. 421–428.
- [17] M. Copeland, G. Slemon, An analysis of the hysteresis motor i-analysis of the idealized machine, *IEEE Transactions on Power Apparatus and Systems* 82 (65) (1963) 34–42.
- [18] S. Miyairi, T. Kataoka, A basic equivalent circuit of the hysteresis motor, *Elect. Engng. Japan (USA)* 85 (1965) 41–50.
- [19] M. Imani Nejad, Self-bearing motor design & control, Ph.D. thesis, Mechanical Engineering, Massachusetts Institute of Technology (2013).
- [20] J. Nitao, E. Scharlemann, B. Kirkendall, Equivalent circuit modeling of hysteresis motors, Tech. rep., Lawrence Livermore National Laboratory (LLNL), Livermore, CA (2009).
- [21] F. A. Zaher, An analytical solution for the field of a hysteresis motor based on complex permeability, *IEEE Transactions on Energy Conversion* 5 (1) (1990) 156–163.
- [22] T. Horii, N. Yuge, G. Wakui, Analysis of a hysteresis motor on asynchronous speed using complex permeability, *IEEE Translation Journal on Magnetics in Japan* 9 (2) (1994) 135–142.
- [23] S. Clurman, On hunting in hysteresis motors and new damping techniques, *IEEE Transactions on Magnetics* 7 (3) (1971) 512–517.
- [24] A. E. Bryson, *Applied optimal control: optimization, estimation and control*, CRC Press, 1975.
- [25] MicroWheel 200 (MW200) reaction wheel, Tech. rep., Microsat Systems Canada Inc. (2001).